

Gate-tunable phase transition in a resonator-based Su-Schrieffer-Heeger chain

Splitthoff, Lukas Johannes; Belo, Miguel Carrera; Jin, Guliuxin; Liu, Yu; Greplova, Eliska; Andersen, Christian Kraglund

DOI

[10.1103/PhysRevResearch.6.043286](https://doi.org/10.1103/PhysRevResearch.6.043286)

Publication date

2024

Document Version

Final published version

Published in

Physical Review Research

Citation (APA)

Splitthoff, L. J., Belo, M. C., Jin, G., Liu, Y., Greplova, E., & Andersen, C. K. (2024). Gate-tunable phase transition in a resonator-based Su-Schrieffer-Heeger chain. *Physical Review Research*, 6(4), Article 043286. <https://doi.org/10.1103/PhysRevResearch.6.043286>

Important note

To cite this publication, please use the final published version (if applicable). Please check the document version above.

Copyright

Other than for strictly personal use, it is not permitted to download, forward or distribute the text or part of it, without the consent of the author(s) and/or copyright holder(s), unless the work is under an open content license such as Creative Commons.

Takedown policy

Please contact us and provide details if you believe this document breaches copyrights. We will remove access to the work immediately and investigate your claim.

Gate-tunable phase transition in a resonator-based Su-Schrieffer-Heeger chain

Lukas Johannes Splitthoff^{1,2,*} Miguel Carrera Belo^{1,2} Guliuxin Jin² Yu Liu³
 Eliska Greplova² and Christian Kraglund Andersen^{1,2}

¹*QuTech, Delft University of Technology, Delft 2628 CJ, The Netherlands*

²*Kavli Institute for Nanoscience, Delft University of Technology, Delft 2628 CJ, The Netherlands*

³*Center for Quantum Devices, Niels Bohr Institute, University of Copenhagen, 2100 Copenhagen, Denmark*



(Received 29 April 2024; accepted 9 October 2024; published 16 December 2024)

Metamaterials engineered to host topological states of matter in controllable quantum systems hold promise for the advancement of quantum simulations and quantum computing technologies. In this context, the Su-Schrieffer-Heeger (SSH) model has gained prominence due to its simplicity and practical applications. Here we present the implementation of a gate-tunable, five-unit-cell resonator-based SSH chain on a one-dimensional lattice of superconducting resonators. We achieve electrostatic control over the inductive intracell coupling using semiconductor nanowire junctions, which enables the spectroscopic observation of a transition from a trivial to a topological phase in the engineered metamaterial. In contrast to prior work, our approach offers precise and independent *in situ* tuning of the coupling parameters, which is critical to directly approximate ideal tight-binding Hamiltonians via the control over local variables. Our results supplement efforts towards gate-controlled superconducting electronics and large controllable resonator-based lattices to enable quantum simulations.

DOI: [10.1103/PhysRevResearch.6.043286](https://doi.org/10.1103/PhysRevResearch.6.043286)

I. INTRODUCTION

Metamaterials are engineered structures of simple constituents, which exhibit functionalities that go beyond those of the individual building blocks. For quantum systems, this transferable concept of metamaterials can be used to engineer materials that host topological states of matter which remain robust against imperfections and are therefore suited for quantum computing and simulation [1,2]. Recently, there has been great interest in topological metamaterials that resembles the Su-Schrieffer-Heeger (SSH) model [3–7]. The SSH model predicts a phase transition of a finite, $2N$ -site chain with alternating coupling strength between a band insulator and a topological insulator with localized edge states. The SSH model finds applications in the entanglement stabilization of quantum states [8], the long-range interaction of qubits [9–12] and the study of non-Hermitian light-matter interaction [13–15].

Due to the generality of the concept, topological metamaterials can be realized in various material platforms and efforts materialized in spin qubits [16], Rydberg atoms [17], adatoms [18] and integrated photonics [19]. The idea has also been taken to classical electrical circuits made out of surface mount components on printed circuit boards [20–22]. However, to fully observe a topological phase transition in a metamaterial, achieving control over local variables in tight-

binding models is critical and previous works have so far not demonstrated such capabilities. To address this challenge, we will here focus on superconducting quantum circuits, which has emerged as one of the leading platforms for quantum simulation and computation [23]. Thanks to the mature fabrication and design techniques of superconducting circuits, the reliable large-scale implementation of superconducting qubits and resonators is feasible which led to a number of experiments with engineered photonic baths [24–34], topological electrical circuits [35,36], and qubit-to-topological waveguide coupling [7,10,37–39].

While all of the aforementioned efforts resemble static realizations of metamaterials, the engineering of topological metamaterials from superconducting circuits with tunable spectral bandgap and controllable interaction remains an open challenge due to the necessary integration of multiple tunable elements with low cross-talk. Those efforts would enable quantum simulation of novel states of matter [40,41] or the development of new circuit components such as on-chip isolators [42] or long-range couplers. The required tunability could be provided via flux-controlled SQUID loops [43–45] or current biased conductors [46–49]. However, both control methods unavoidably introduce crosstalk between ideally independent tunable elements due to long-range magnetic field lines or supercurrents affecting SQUID loops or current biased conductors. This crosstalk poses a major control issue and significantly complicates the device tune-up, since achieving full control requires prior crosstalk calibration and subsequent compensation [50–52]. Especially in the context of tight-binding model simulations, the crosstalk calibration necessitates the challenging reconstruction of local Hamiltonian parameters. Although precise topological Hamiltonian reconstruction is possible [53], the required amount of training data is typically high. Moreover, the topological nature of the

*Contact author: l.j.splitthoff@gmail.com

Published by the American Physical Society under the terms of the [Creative Commons Attribution 4.0 International](https://creativecommons.org/licenses/by/4.0/) license. Further distribution of this work must maintain attribution to the author(s) and the published article's title, journal citation, and DOI.

model creates a challenge for the Hamiltonian reconstruction because the measurement results can be less sensitive to parameter variation compared to trivial phases. To alleviate the need for advanced control strategies and eliminate crosstalk between mesoscopic circuit elements, one could instead leverage the local control over the microscopic properties of circuit elements. Such source of tunability became available with the local electrostatic control of the supercurrents in hybrid superconducting semiconducting structures [54–58] or other hybrid structures, which should enable the crosstalk-free integration of tunability. Based on this concept of gate-tunability, gate-tunable transmon qubits [54,56], bus resonators [55] and parametric amplifiers [58,59] have been realized in previous work.

In this work, we present a topological metamaterial with gate-tunable coupling within each unit cell. Specifically, we implement a five-unit-cell resonator-based SSH chain composed of two resonators per unit cell forming a one-dimensional lattice of ten superconducting resonators. By taking the idea of electrostatic control from the single element level, as in a gatemon device, to scale, we achieve *in situ*, electrostatic control over several inductive intracell coupling elements using semiconductor nanowire junctions, which enables the spectroscopic observation of a trivial-to-topological phase transition in the engineered topological metamaterial.

II. SSH CHAIN IMPLEMENTATION

We implement the five-unit-cell tight-binding SSH model, as shown in Fig. 1(a), using a chain of 10 lumped-element, high-kinetic inductance, superconducting resonators with alternating variable inductive intracell coupling v and static capacitive intercell coupling w , see Fig. 1(b). One unit cell, see Fig. 1(c), is composed of two resonators with intracell coupling v . The capacitive intercell coupling is set by the geometry of the neighboring resonators between unit cells. The inductive intracell coupling is realized by five gate-tunable Josephson junctions formed in five proximitized semiconducting nanowires, which intraconnect the two resonators of a unit cell.

The resonators are made from a high kinetic inductance film to reduce their footprints and avoid spurious modes. Within a unit cell, the resonators are spatially separated to minimize the residual capacitive intracell coupling and are arranged in a mirrored configuration to suppress the residual capacitive second-nearest-neighbor coupling and residual mutual inductances between neighboring sites. The chain is terminated to either side by resonator-like coupling sites with an open inductor to maintain a coupling strength w on both ends to preserve the chiral symmetry. These coupling sites themselves connect directly to the input port S and the output port D, which enable transmission measurements.

The equivalent circuit model of a single unit cell is shown in Fig. 1(c) displaying the four relevant circuit parameters: the resonator capacitance C_0 , the resonator inductance L_0 , the capacitive intercell coupling C_w , and the inductive intracell coupling L_v on the two sublattice sites A and B. The relation between v and L_v and between w and C_w is discussed in Appendix A. In this approximation we neglect the residual

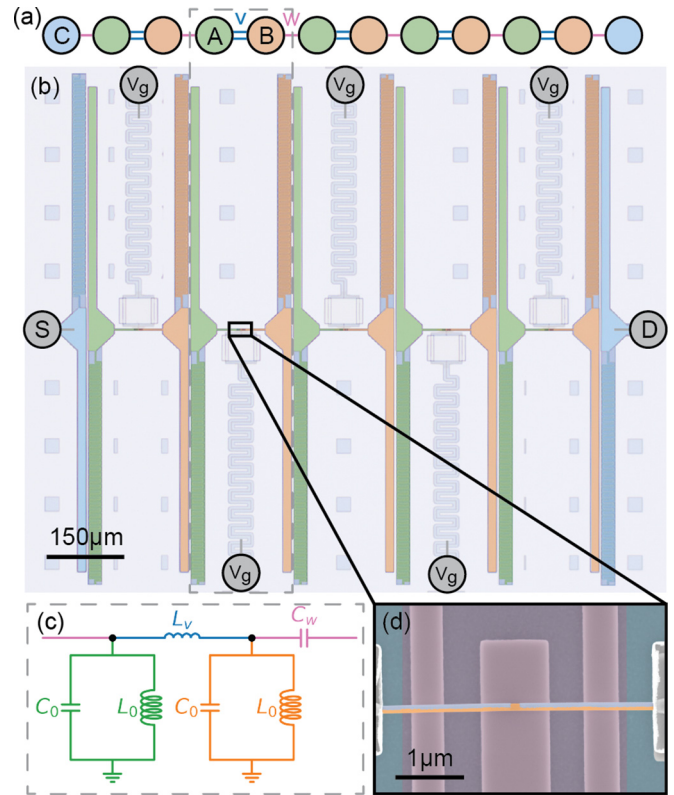


FIG. 1. Superconducting resonator-based SSH chain implementation. (a) Illustration of the SSH tight-binding model with two-site unit cell A-B, intracell coupling v , and intercell coupling w . The finite chain is terminated to coupling sites C. The gray box highlights one unit cell. (b) False-colored microscope image of the five unit cell SSH chain composed of lumped element resonators with alternating variable inductive coupling and static capacitive coupling. The chain is measured from port S to port D in transmission. The inductive coupling, mediated by proximitized nanowire Josephson junctions, is controlled via five independence voltage gates. One unit cell is highlighted within the dashed box as in panel (a). (c) Equivalent circuit of a single unit cell in (b). The individual circuit elements are discussed in the main text. (d) False-colored micrograph images of a single gate controlled proximitized nanowire Josephson junction. Orange: InAs semiconductor, blue: Al thin film, purple: SiN gate dielectric on NbTiN gate electrodes, turquoise: Si substrate, gray: NbTiN contacts.

capacitive intracell C_v and the residual capacitive second-nearest-neighbor coupling C_{SNN} .

As mentioned, the inductive coupling are realized using nanowire Josephson junctions as shown in the zoomed in picture in Fig. 1(d). The gate voltages are applied via Chebyshev-filtered gate lines [see Fig. 1(b)] and control the Andreev bound states carrying the super-current between the superconducting leads of the nanowire junctions separately by changing the chemical potential which in turn set the respective Josephson energies E_J . Eventually, the coupling inductance is then given by the Josephson inductance $L_v(V_g) = \phi_0(2\pi I_c(V_g))^{-1} = \phi_0^2(E_J(V_g))^{-1}$, where I_c is the gate-tunable critical current, E_J the gate-tunable Josephson energy and $\phi_0 = h/2e$ the magnetic flux quantum. The inductance approaches infinite when the nanowire Josephson junction gated

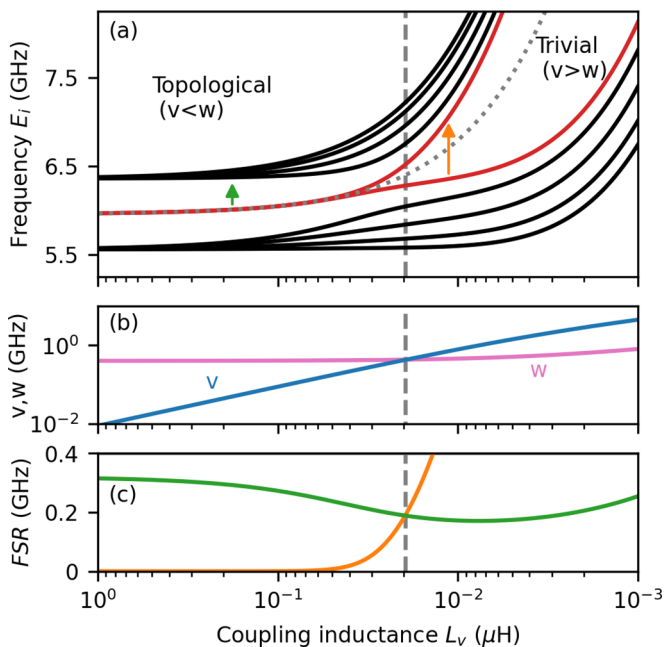


FIG. 2. Simulated spectrum versus the coupling inductance L_v of a resonator-based SSH chain with the circuit parameters used in the experiment. (a) Energy spectrum of the bulk modes (black) and the edge modes (red) versus the coupling inductance L_v . The dashed line indicates the phase transition point between the topological and the trivial phase where $v = w$. The gray dotted line indicates the instantaneous resonator frequency ω_r . (b) Coupling coefficients v (blue) and w (pink) versus coupling inductance L_v . (c) Free spectral range FSR between the edge states and the bulk (green, arrow in (a)) and between the two edge modes (orange, arrow in (a)).

below the pinched-off voltage $V_g < V_p$, and it is finite on the order of a few nano-Henry otherwise when charge carriers are accumulated in the junction region. Physically, the junction is composed of thin aluminum film on two facets of the InAs nanowire which has been selectively etched to form a 110-nm-long Josephson junction. The junction directly connects to resonators on either side via NbTiN contacts. The voltage gate is surrounded by two narrow ground lines to ensure equal ground potentials on the upper and lower half of the SSH chain.

Our circuit implementations shares the same tight-binding geometry as the SSH model with identical on-site potentials and alternating coupling strengths v and w , as highlighted with a corresponding color code in Figs. 1(a) and 1(b). To further affirm the correspondence between the SSH model and our implementation we derive the real-space Hamiltonian from the circuit Lagrangian (see Appendix A 3). The diagonalization of the real-space Hamiltonian for realistic circuit parameters yields the eigenvalues for uniformly varied coupling strength L_v , see Fig. 2.

As shown numerically in Fig. 2(a) for 10 circuit modes, in the case of large inductances, $L_v > 19$ nH corresponding to $v < w$, the spectrum exhibits two nearly degenerate midgap modes (red) centered around the eight bulk modes (black). Such midgap modes are the characteristic feature of a topological insulator state. Hence, we find the system to be in the topological insulator state if the nanowire junctions are

pinched-off. As the coupling inductance decreases, so that the coupling strength v increases by more than two orders of magnitude and the coupling ratio crosses over to $v > w$, see Fig. 2(b), the midgap modes split and approach the bulk modes, which eventually leads to a fully gaped spectrum corresponding to the trivial insulator state. Particular for this implementation is the frequency shift of the entire spectrum for smaller coupling inductances as the change in L_v also renormalizes the on-site potential, here the resonator frequency ω_r . Consequently, also w increases slightly following the increase in ω_r as seen in Fig. 2(b). Note that the spectrum remains symmetric around the instantaneous resonator frequency ω_r indicated by the gray dotted line in Fig. 2(a). (see also Appendix A 3 b), which is characteristic for a system obeying chiral symmetry [5]. To highlight the spectral evolution further, we present the free spectral range (FSR) between one midgap mode and the nearest bulk mode as well as the separation between the two midgap modes in Fig. 2(c), which quantifies the energy splitting between adjacent modes. The system undergoes a phase transition between the topological and the trivial state as the order of the coupling strength v and w inverts. At the point where $v = w$, the FSR between the midgap modes and the nearest bulk modes are equal, see Fig. 2(c), but remains finite due to the finite system size. We refer to this intermediate state with approximately equal FSR as a normal state, which would correspond to the point of the gap-closing for systems in the thermodynamic limit.

Despite the presence of on-site and coupling strength disorder in this simulation, which represents the actual experimental circuit implementation, the spectrum is nearly indistinguishable from an ideal SSH chain, which shows the robustness of this implementation method. The only difference appears in the symmetry of the bulk modes (see Appendix A 2).

III. OBSERVATION OF PHASE TRANSITION

We experimentally resolve the energy spectrum of the 10 site SSH chain implementation via a transmission measurement at microwave frequencies through the chain from port S to port D for different gate voltages applied to nanowire junctions measured at the base temperature of a dilution refrigerator. In this measurement, eigenmodes of the SSH chain manifest as peaks in the transmission spectrum. Their linewidth is proportional to the respective wave-function weight on the outer sites of the chain $|\psi_{0,2N}|^2$.

By pinching off the Josephson junctions, the intracell coupling v is minimized and we measure the spectrum with a gate voltage of $V_g = -1$ V on all gates. As shown in Fig. 3, we observe a transmission spectrum with nine peaks corresponding to the eight bulk modes and the two quasidegenerate edge modes occupying the lower band, the gap, and the upper band of the spectrum. The red crosses indicates the frequency points of the individual modes. As discussed, the linewidth of a mode depends on its coupling strength to the measurement ports. Hence, modes with more wave-function weight on lattice sites close to the edge of the chain couple more strongly to the measurement ports and appear as broader modes in the spectrum. Following this argument, we assign the narrow

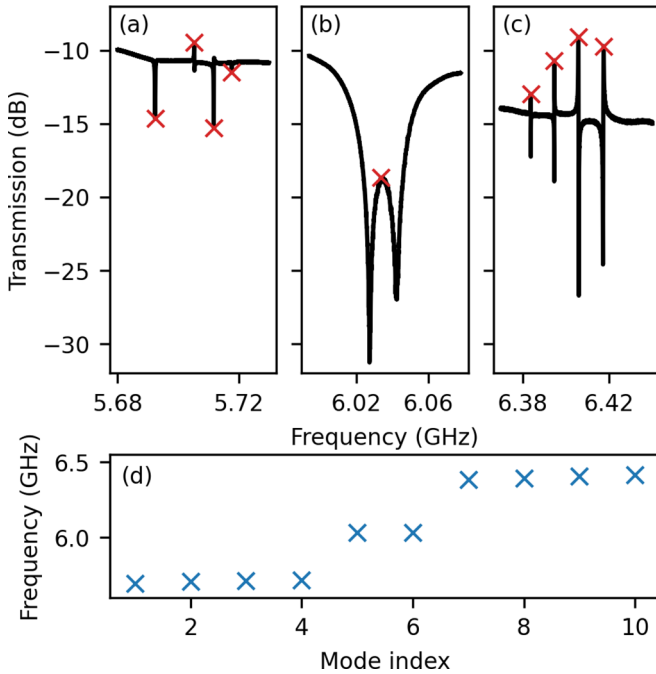


FIG. 3. Parameter estimation of the SSH chain in the topological phase. [(a)–(c)] Transmission spectrum of the lower band, the gap and the upper band. The red crosses mark the 10 modes of the five unit cell SSH chain. (d) Eigenfrequency of the 10 modes in the topological phase sorted by mode index.

modes in ranges 5.68–5.72 GHz and 6.38–6.42 GHz as bulk modes. The wider, central peak around 6.04 GHz then corresponds to the quasidegenerate midgap modes. The reduced transmission amplitude of the midgap modes compared to the maximal transmission results from the localization on either site of the chain. The asymmetric and distorted lineshapes of the SSH chain modes originate from Fano resonances of these relatively narrow modes with a broad spectral feature centered around 6 GHz formed by the sample mount.

The sorted eigenfrequencies versus mode index in Fig. 3(d) shows the gaped spectrum with quasidegenerate zero energy modes, which is characteristic for the topological insulator state expected for this system. After the mode assignment, we can estimate the on-site energies and the coupling strength of each individual site along the SSH chain to obtain an estimate of the circuit parameters by fitting the full 10-dimensional Hamiltonian to the extracted eigenfrequencies (see Appendix B). The average values of the estimated circuit parameters C_0 , L_0 , C_w , and L_v deviate from the design parameters by less than 10%. Moreover, we find a parameter disorder of less than 1% along the chain. The obtained parameters were used to generate the simulated data shown in Fig. 2.

Having established the circuit parameters in the topological regime, we now leverage the tunability per unit cell to observe the topological phase transition predicted for the SSH model. We first characterize the gate dependence of each individual nanowire junction, which is a critical requirement in order to unambiguously control local variables in Hamiltonian simulations aiming to observe topological features and localization effects in tight-binding models. Specifically,

we record the spectrum for a wide range of gate voltages per nanowire junction to identify the pinch-off voltage V_{p_i} that suppresses the supercurrent across each junction and the open voltage V_{o_i} that maximizes the supercurrent of the junction, see also Appendix C. The acquired gate dependencies per nanowire junctions correspond well to their respective tight-binding simulation, which suggests negligible crosstalk between nearby voltage gates. Next, we measure the energy spectrum of the SSH chain along a synchronous evolution of the coupling inductances L_v as we linearly interpolate each junction between V_{o_i} and V_{p_i} . We assume that each nanowire junction opens at a similar rate between V_o and V_p such that the joint gate control mimics the synchronous tuning of L_v in all junctions. The resulting spectrum over 1 GHz with a 70 kHz resolution in the few photon regime versus a synchronous gate setting scan is shown in Fig. 4(a) after background correction (see Appendix G). Three linecuts, colored relative to their respective gate setting in Fig. 4, exhibit three different regimes of the SSH chain and demonstrate that we can experimentally access each regime with *in situ* tuning.

The spectral fan-out and overall increase of the eigenfrequencies of the SSH modes with increasing gate voltages, hence decreasing coupling inductances, qualitatively follows the simulation presented in Fig. 2(a). For the initial gate settings close to V_p shown in Fig. 4(b), we obtain a gaped spectrum with midgap modes and a free spectral range of $\text{FSR} = 350$ MHz, which we previously identified as topological insulator state. As the gate voltages increase towards V_o , the initially quasidegenerate midgap modes with relatively wide linewidth and maximal prominence split and approach the lower and upper bundle of four modes. Eventually, close to V_o , the lines in the spectrum form two bundles of five modes each, are narrow in linewidth and of low prominence, see Fig. 4(d). We identify this single gaped spectrum with a free spectral range of $\text{FSR} = 240$ MHz as trivial insulator state. Note that the two highest mode in Fig. 4(d) exceed the measurement window.

Aside from the spectroscopic state identification based on the distribution of the eigenmodes, the large prominence of the transmission signal relates to a strong delocalization of the modes while their narrow linewidth is set by the weak coupling to the coupling ports, and vice versa. Hence, the phase transition of the SSH chain manifests in this experiment in the FSR and the linewidth of the modes: (i) Starting from the topological insulator state, the FSR between the midgap modes and the nearest bulk modes continuously closes while FSR between the initial midgap modes widens. Around the phase transition the system passes through an intermediate, normal regime corresponding to the trace in Fig. 4(c), where the FSR between the midgap modes and the FSR to the nearest bulk modes is approximately equal. This change in FSR is in qualitative agreement with the simulated trend shown in Fig. 2(c). (ii) The narrower linewidth together with the larger transmission amplitude of the initial midgap modes indicate that these modes transition from a state localized to the edges of the chain to a delocalized state along the chain as the nanowire junctions open. Moreover, as it can be seen from the comparison of Figs. 4(b) and 4(d), the bulk mode resonances widen from the topological to the trivial state (see Appendix D).

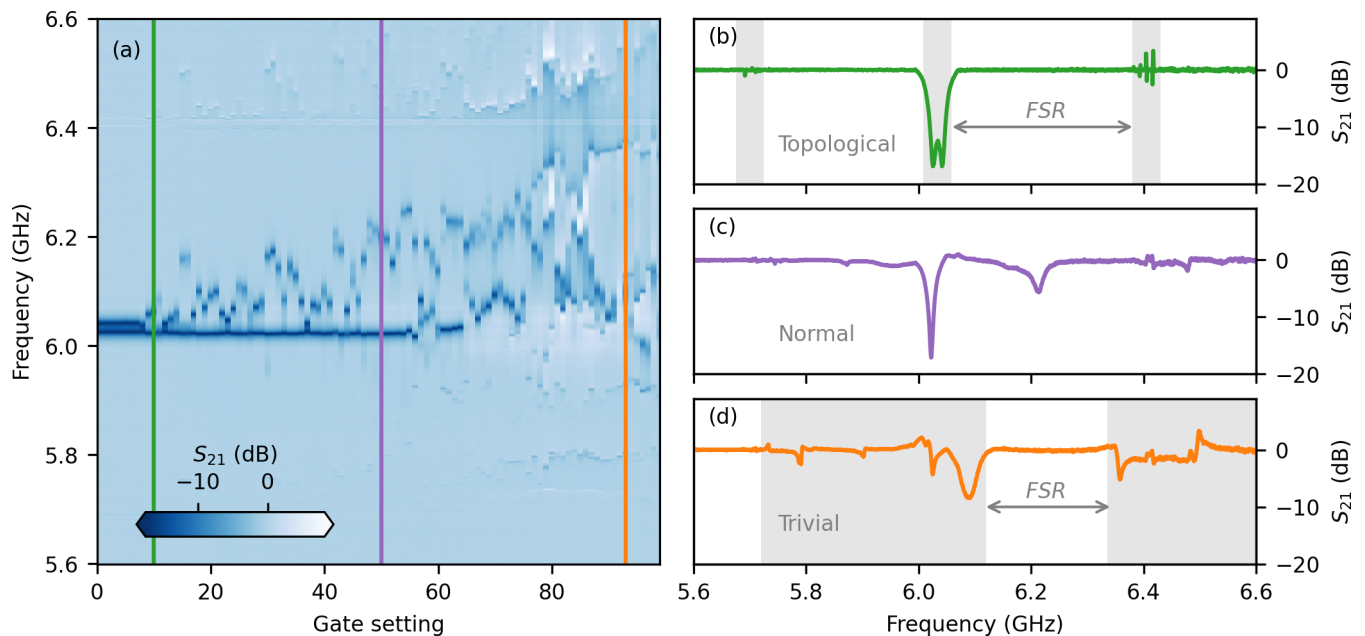


FIG. 4. Gate-tunable phase transition. (a) SSH chain spectrum versus individual gate voltage V_{g_i} aggregated in a joint gate setting sweep (more information in the main text). The shades indicate the normalized S_{21} transmission through the chain. [(b)–(d)] SSH chain spectrum for a given gate setting indicated as colored line in (a). The grayed out regions in (b) and (d) highlight the width of the bands. The arrows indicate the largest free spectral range FSR in these traces.

Beyond these two indicators of the phase transition, we also numerically calculate a topological invariant for the system, see Appendix A 3. Specifically, we calculate the real-space winding number (RSWN) [60–63] and find a nonzero value in the topological regime ($\nu \approx 0$) while the RSWN approaches zero for more open junctions (increasing ν). The finite size of the system prohibits a sharp transition between the two regimes, but the RSWN calculations verify that the limiting cases of pinched off and fully open represent two topologically distinct phases.

While the nonlinear frequency shift of the system is not directly related to the phase transition and kept small by choosing a low probe power, it serves as additional tool to verify that the nanowire junctions are open. While the system in the topological regime remains nearly unchanged versus changes in the probe power, the system frequencies lower drastically with power in the trivial regime due to added Kerr nonlinearity arising from the presence of the open Josephson junctions (see Appendix E).

A caveat, however, remains arising from the nature of nanowire Josephson junctions. As observed in earlier work on nanowire Josephson junctions [54,64–66], the functional dependence of the inductance on the individual gate voltage is highly nonmonotonic and hysteretic over time, which prevents us from observing a smooth phase transition. The effect of disorder and disorder-induced phase transitions can further be studied, following ideas presented in Refs. [60,67,68]. To further address the model accuracy, we estimate the residual second-nearest-neighbor (SNN) and ν coupling capacitances to be $C_{\text{SNN}} = 0.4$ fF and $C_\nu = 0.5$ fF from finite-element simulations, which are two to three orders of magnitude smaller than the coupling capacitance $C_w = 32$ fF and the resonator capacitance $C_0 = 206$ fF. The finite and constant coupling

capacitance C_ν , which is in parallel with L_ν , yields a finite but negligible offset in the coupling strength ν , but does not change the topology of the system. The small second-nearest neighbor coupling C_{SNN} , which connects same sublattice sites, weakly breaks chiral symmetry, as discussed in Ref. [67–69], but parameters, such as the FSR of the midgap modes and the localization of the wave functions in the topological regime remain experimentally indistinguishable from a system with chiral symmetry.

IV. CONCLUSION

We have realized a macroscopic SSH chain out of a one-dimensional lattice of superconducting resonators, which inherits the tunability from the microscopic properties of nanowire Josephson junctions. We have characterized the system in the topological regime and mapped our resonator-based implementation onto the original spin-less, single-particle SSH Hamiltonian. Eventually, we leveraged the unit cell tunability with negligible crosstalk and the engineered robustness against disorder to control the extended states along the SSH chain, which lead to the observation of the topological insulator phase transition in the macroscopic, gate-tunable resonator-based SSH chain from the topological to the trivial insulator phase.

Our experiment takes the idea of gate-tunable superconducting circuits [70] from a single gate-tunable element to scale and demonstrates that the implementation of several nanowire Josephson junctions in circuit QED experiments is possible. This result encourages further research on gate-tunable qubits, such as $\cos(2\phi)$ gatemon qubits [71], Andreev spin qubits [66], or Kitaev chain qubits [72,73]. Also the

number becomes an ill-defined invariant. Alternatively, the covariant real-space winding number (RSWN) serves as a good approximation for the momentum-space winding number given the large enough system size, and the RSWN remains quantized in the presence of disorder [60–63]. In the following, we review the calculation of real-space winding number.

For a one-dimensional chiral symmetric system, recall the anticommutation relation between the Hamiltonian H and the chiral operator Γ in Eq. (A2). This relation results in the fact that the Bloch Hamiltonian $H(k)$ takes the off diagonal form [88]

$$H(k) = \begin{pmatrix} 0 & h(k) \\ h(k)^\dagger & 0 \end{pmatrix}. \quad (\text{A6})$$

The winding number is given by [88]

$$\nu = \frac{1}{2\pi i} \int_{\text{BZ}} \text{Tr}\{[h(k)^{-1} \partial_k h(k)]\} \in \mathbb{Z}. \quad (\text{A7})$$

Equation (A7) has a direct covariant form in the real space [60]. Starting from the real-space SSH Hamiltonian H , the homotopically equivalent flatband version of H is given by

$$Q = \frac{H}{|H|} = \begin{pmatrix} 0 & Q_0 \\ Q_0^\dagger & 0 \end{pmatrix}, \quad (\text{A8})$$

where the off-diagonal part Q_0 enters the calculation of real-space winding number. The covariant real-space form of the winding number can be obtained by applying the Bloch-Floquet transformation of Eq. (A7) written in terms of flatband Hamiltonian [60]

$$\nu = -\text{Tr}_{\text{volume}} \{Q_0^{-1} [X, Q_0]\}, \quad (\text{A9})$$

where X is the position operator and $\text{Tr}_{\text{volume}}$ denotes the trace per volume. In the case of SSH model, the off-diagonal term Q_0 can be obtained as the following. The position eigenstates are $|x, c\rangle$, where $x = 1, \dots, L$ denote the unit cells and $c = A, B$ are the sublattice degree of freedom. The position operator therefore takes the form $X = \sum_{x \in \mathbb{Z}} \sum_{c=A,B} x |x, c\rangle \langle x, c|$. In order to obtain Q_0 , we define spectral projectors as

$$P_A = \sum_{x \in \mathbb{Z}} \sum_{c=A} |x, c\rangle \langle x, c|, \\ P_B = \sum_{x \in \mathbb{Z}} \sum_{c=B} |x, c\rangle \langle x, c| = \hat{I} - P_A. \quad (\text{A10})$$

The chiral operator Γ is given by $\Gamma = P_A - P_B$. In parallel, we define the projectors onto the upper and lower half of the energy spectrum

$$P_- = \sum_{E_n \leq 0} |n\rangle \langle n|, \\ P_+ = \sum_{E_n \geq 0} |n\rangle \langle n| = \Gamma P_- \Gamma. \quad (\text{A11})$$

Then the flatband Hamiltonian in Eq. (A8) can be obtained by $Q = P_+ - P_-$. As a chiral-symmetric operator, Q satisfies the condition $Q = P_A Q P_B + P_B Q P_A$. The off-diagonal terms in Eq. (A8) can be written in terms of the above defined

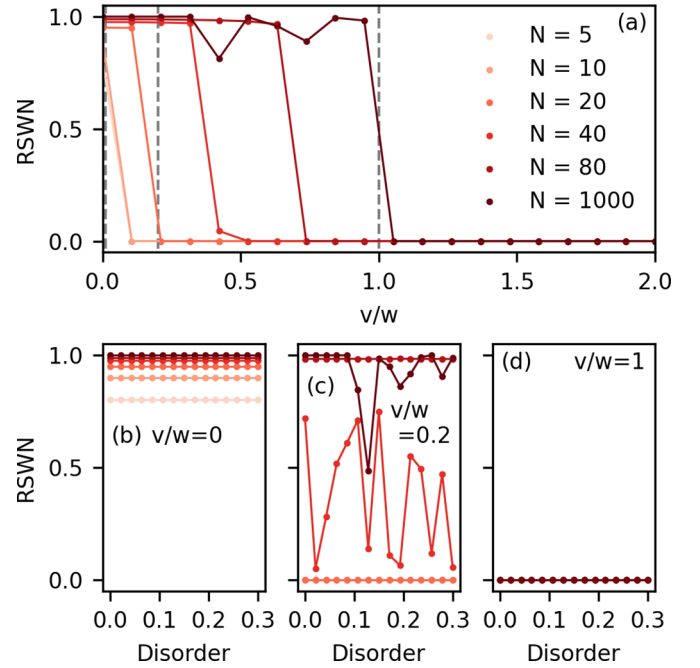


FIG. 6. Real-space winding number. (a) RSWN versus coupling strength ratio. The dashed vertical lines correspond to the v/w ratio used in the disorder simulations shown in (b)–(d). [(b)–(d)] RSWN versus disorder strength for three different coupling strength.

operators as

$$Q_0 = P_A Q P_B, \quad (Q_0)^{-1} = P_B Q P_A. \quad (\text{A12})$$

Finally, one can express real-space winding number Eq. (A9) as

$$\nu = -\frac{1}{L} \text{Tr}\{P_B Q P_A [X, P_A Q P_B]\}. \quad (\text{A13})$$

In our study, we compute the RSWN versus the coupling strength v/w for various chain lengths N and for $w = 0.5$, see Fig. 6(a). On either end of the coupling strength range ($v \in (0, 1)$), the system approaches the topological and trivial state with $\text{RSWN}=1$ and $\text{RSWN}=0$, respectively, regardless of the chain length. In-between $v \in (0, 1)$, the RSWN indicates a crossover between the two different insulator states, but only in the thermodynamic limit $N \rightarrow \infty$ the RSWN correctly predicts the phase transition point as it approximates the k -space winding number. For small N , the RSWN does not capture the phase transition, which is spectroscopically still defined, due to finite-size effects. Additionally, we investigate the robustness of the topological state by examining the RSWN under varying levels of disorder in the coupling parameter v and w for three different intracell couplings $v = \{0.0, 0.2, 1\}$, see Figs. 6(b)–6(d). While the RSWN does not aim at benchmarking the phase transition for our finite-size system, we see that in the limiting cases we have distinct topological phases which providing valuable insights into the topological phase transition that we observe experimentally.

b. Symmetries

To further strengthen the claim that the chiral symmetry persists in the ideal SSH chain implementation, we present

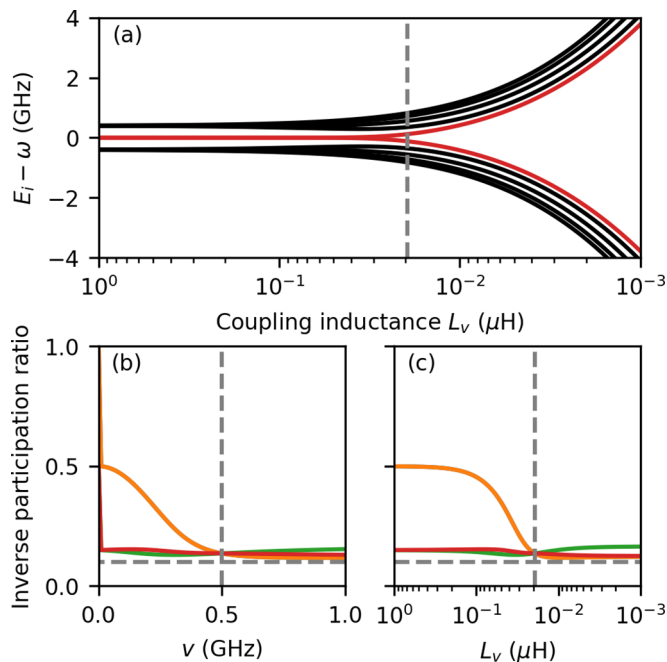


FIG. 7. (a) Normalized simulated spectrum of the resonator-based SSH chain with ideal the on-site and coupling energies as in Fig. 5. [(b) and (c)] Inverse participation ratio for different states for the tight-binding model (b) and the ideal SSH chain implementation (c) versus the coupling strength v . The dashed line indicates the $1/2N$ limit. The colors correspond to the respective wave functions in Fig. 5.

the spectrum of Fig. 5(c) normalized by the instantaneous resonator frequency $\omega(L_v)$ in Fig. 7(a). This normalized spectrum is symmetric around the on-site energy. Moreover, we can compute the anticommutator and find that it vanishes $\{\Gamma, H_{LC}\} = 0$.

c. Localization

The localization of the wave functions of the edge states is a characteristic of the SSH chain. For finite chain lengths, however, the localization length defined as exponential decay $\exp(-x/\xi)$ does not capture the delocalization of the edge modes as the system undergoes the phase transition, as seen in Fig. 5(b). Instead, for finite chain length we can define an inverse participation ratio (IPR) [69], which measures the support of a wave function on a specific site and is defined as

$$\text{IPR} = \frac{\sum_x |\psi(x)|^4}{(\sum_x |\psi(x)|^2)^2}. \quad (\text{A14})$$

We observe that the IPR of the edge modes is finite and larger than for the bulk modes in the topological phase. As the system undergoes the phase transition, the IPR decreases and approaches the delocalization limit $1/2N = 1/10$ of the bulk modes at $v = w$, see Figs. 7(b) and 7(c). The IPR of the localized modes is of value one only in the fully dimerized case $v/w = 0$, hence we observe a kink in the IPR in Fig. 7(b) close to $v = 0$.

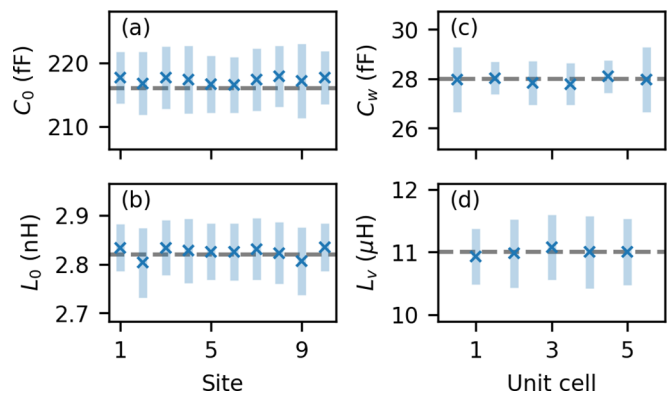


FIG. 8. Extracted circuit parameters in the topological phase. [(a) and (b)] Resonator capacitance C_0 and inductance L_0 per site. [(c) and (d)] Coupling capacitance C_w and coupling inductance L_v per coupling site.

APPENDIX B: CIRCUIT PARAMETER ESTIMATION

From the presence of the bulk and gap modes in the spectrum for a given L_v configuration, we can extract the circuit parameters C_0 , L_0 , C_w , and L_v . First, we identify and list the eigenmodes of the system. Then, we fit the 10-dimensional Hamiltonian H_{LC} to the list of eigenmodes while allowing for free variation of all circuit parameters along the chain. For completeness, we also take the two C_w couplings to the coupling sites C into account, which expands the C_w list from four to six elements. Since the eigenfrequencies of the coupling sites are far detuned from the SSH spectrum, we do not consider them in the system Hamiltonian. The circuit parameters obtained from this optimization routine in the topological phase are shown in Fig. 8. We assume the design parameters as start parameters for the Nelder-Mead optimization. The variation of the obtained parameters is smaller than 1%. Finally, we input the obtained circuit parameters into the full Hamiltonian to compute the spectrum and the eigenstates to simulate the data in Figs. 2 and 3(d). The agreement of this optimization with the measurement results is on the order of a few kHz, which is also the spectral resolution of the measurement. This parameter estimation yields the static parameters C_0 , L_0 , and C_w . The optimization routine can then in principle be repeated for different L_v configurations to the trivial phase.

From finite-element simulations in COMSOL we estimate the residual capacitances to be $C_{SNN} = 0.4$ fF and $C_v = 0.5$ fF, which are two to three orders of magnitude smaller than the coupling capacitance $C_w = 32$ fF and the resonator capacitance $C_0 = 206$ fF. Hence, we neglect the contribution of the residual capacitances in the parameter extraction. Moreover, including the residual capacitances yields more uncertainty in the circuit model reconstruction given the limited sensitivity to small C_v and C_{SNN} as well as the limited number of 10 eigenmodes we can fit the model to.

While any on-site disorder and second-nearest-neighbor interaction due to residual capacitive coupling breaks the chiral symmetry, strictly speaking, the midgap modes remain localized and can therefore be understood as chiral for practical purposes [69].

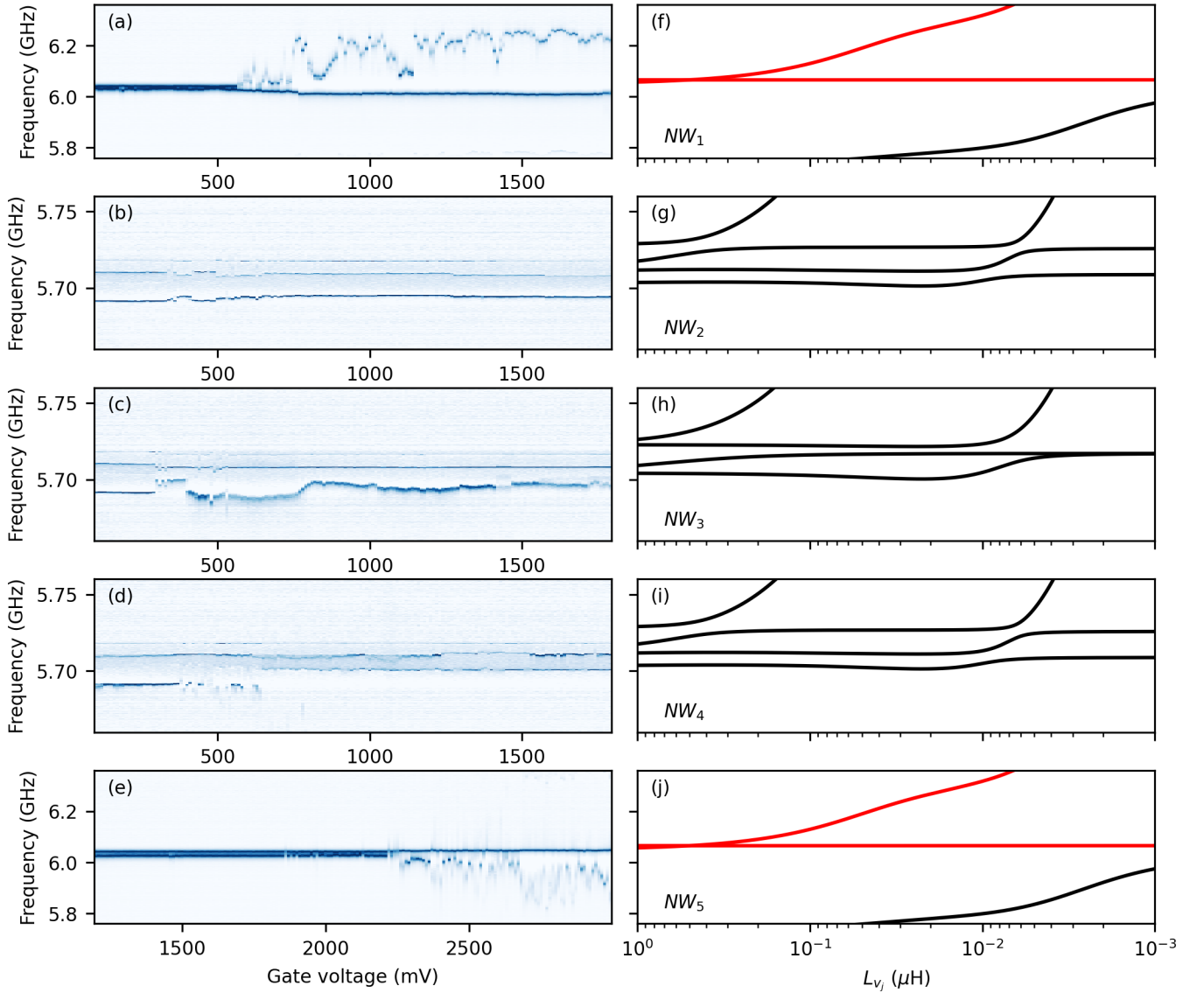


FIG. 9. Single gate dependence. [(a)–(e)] Measured spectrum per gate while the other gates are set to V_p . Zoom-in on low band for bulk gates and zoom-in on gap for edge gates. The data is normalized on the background to enhance the visibility of the change. [(f)–(j)] Corresponding simulated spectrum.

APPENDIX C: SINGLE GATE DEPENDENCE

A transmission measurement through the five unit cell SSH chain allows for a site specific tune-up of every tunable coupling element. We run single gate scans for every nanowire Josephson junction over a wide gate voltage range, while we keep all other gates at the pinch-off voltage V_p , see Figs. 9(a)–9(e). Hence, all scans begin deep in the topological regime. For the bulk gates NW_i with $i \in [2, 3, 4]$ we zoom on the low band in the topological state, while we focus on the gap for the edge gates NW_i with $i \in [1, 5]$, as we expect the biggest change in frequency in those spectral ranges.

We notice the nonmonotonic single gate dependence of the modes in the respective test spectrum due to microscopic properties, most likely spurious quantum dots in the 100-nm-long junction. In fact, we observe discontinuities due to jumps in the microscopic properties of the junctions. Repetitions of these scans reveal that the slopes change over time. Hence,

even these single gate dependencies cannot be used to calibrate for a joint gate scan across the phase transition point with identical nanowire inductances along the SSH chain.

The measured single gate dependencies are in qualitative agreement with the simulated spectra on the right of Fig. 9. From the single gate dependencies we can extract the voltage V_o , which corresponds to the maximal supercurrent, hence minimal L_J or, expressed in Josephson energy, maximal E_J . This voltage point seem robust enough and constant over time and over several gate scans.

APPENDIX D: ADDITIONAL JOINT GATE DEPENDENCE

In Fig. 10, we repeat the measurement shown in Fig. 4 over the gate settings V_p and V_o defined as minimal and maximal value of the single gate dependencies shown in Fig. 9 at -30 dBm signal power. The splitting of the modes with increasing gate voltage, thus higher gate setting index,

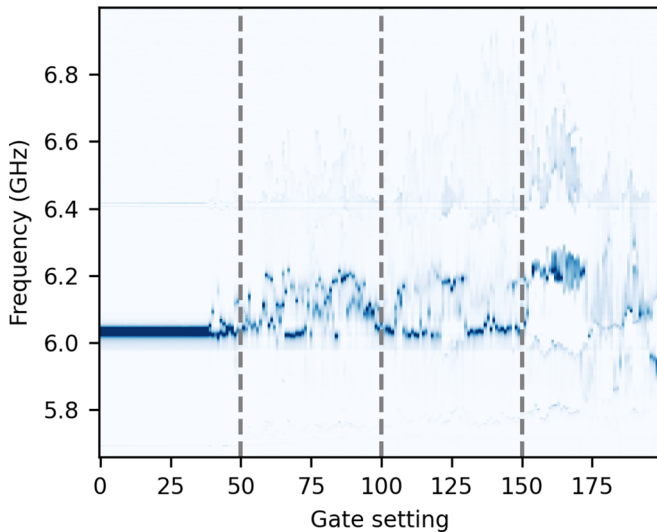


FIG. 10. Additional joint gate dependence with V_p and V_o taken as minimal and maximal value of the single gate dependencies shown in Fig. 9. The dashed lines indicate the gate settings used for the power dependence shown in Fig. 11.

is in qualitative agreement with the equivalent scan from an earlier cooldown presented in Fig. 4, which uses similar gate settings $V_p = [400, 150, 430, 400, 1900]$ mV and $V_o = [1800, 1800, 1800, 1800, 4000]$ mV for the nanowire gates 1 to 5.

APPENDIX E: POWER-INDUCED PHASE TRANSITION

Figure 11 shows the midgap spectrum versus signal power at the signal generator output for three gate voltage settings corresponding to the three gate settings [50, 100, 150] in Fig. 10, (a) close to the topological regime, (b) close to the normal regime, and (c) deep in the trivial regime. The dark lines on the light background indicate the midgap modes. We observe that the two modes are quasidegenerate at high signal powers and the spectrum is nearly indistinguishable from the topological regime regardless of the exact gate setting. As we reduce the signal power, the two modes split and approach the low power spectrum shown in Fig. 10. In the low power regime, the spectral evolution exhibits a gate dependence. For a gate set-point deep in the topological regime, the modes do not disperse with signal power (not shown here). We understand this power-induced phase transition as a result of the power-dependent change in the kinetic inductance of the proximitized nanowires. The inductance in these nanowires follows the equation

$$L_{\text{NW}} = L_0(V_g) \left[1 + \left(\frac{I_s}{I_*(V_g)} \right)^2 \right], \quad (\text{E1})$$

where $L_0(V_g)$ is the gate-dependent low-power inductance, I_s is the signal current through the chain, and $I_*(V_g)$ is the gate-dependent critical current. The signal power enters the equation via the signal current to which it is proportional $P_s I_s^2$. Hence, an increasing signal power increases the inductance, which in turn transitions the SSH chain into the topological regime. The nonmonotonic power dependence as well as the

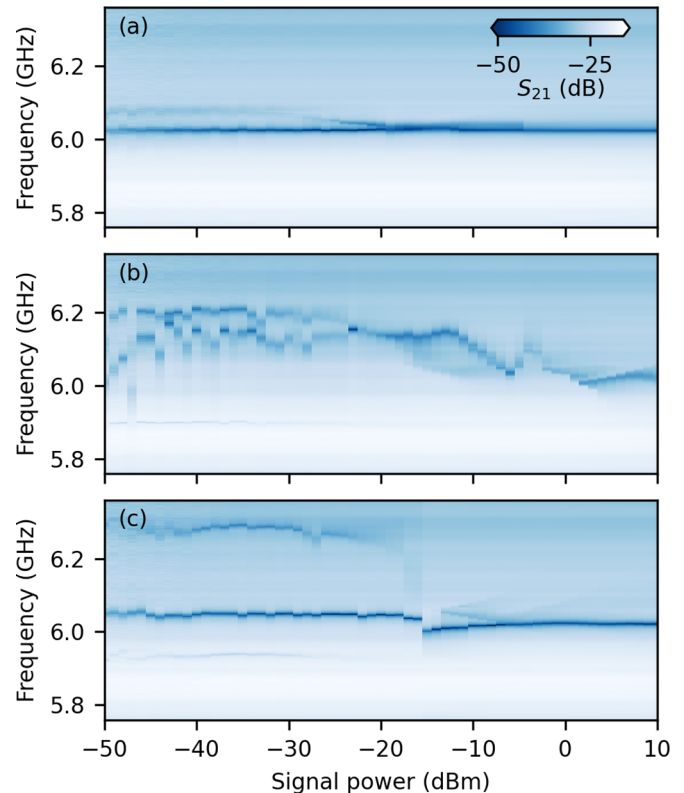


FIG. 11. Power-induced phase transition. [(a)–(c)] Mid-gap spectrum versus signal power at the signal generator output for the three gate voltage settings [50, 100, 150] in Fig. 4.

different transition points most likely arise from the different critical currents $I_*(V_g)$ per nanowire. Consequently, in order to recover the SSH spectrum versus gate voltage, the measurements must be acquired with a signal power below -30 dBm.

APPENDIX F: FABRICATION

We fabricate the SSH chain circuit and the gate lines from a 40-nm-thick sputtered NbTiN film (kinetic inductance $4 \text{ pH } \square^{-1}$) on high resistivity n -doped Si. We pattern the NbTiN film using e-beam lithography and SF_6/O_2 -based reactive ion etching. 30 nm-thick plasma enhanced chemical vapor deposition SiN defined by a buffered oxide etch serves as bottom gate dielectric. We transfer the two-facet InAs/Al nanowire on top of the SiN bottom gate using a nanomanipulator. The InAs nanowires were grown by vapor-liquid-solid growth with a diameter of 110(5) nm, and nominal thickness of the Al of 6 nm [89]. We selectively etch the 110-nm-long Josephson junctions into Al film. Then, we electrically contact the nanowires to the circuit via lift-off defined 150-nm-thick sputtered NbTiN leads after prior Ar milling to minimize the contact resistance.

APPENDIX G: SSH CHAIN ENVIRONMENT

We measure the transmission spectrum of the SSH chain in the topological state over the accessible frequency range (4–8 GHz), see Fig. 12. We observe a peaked background

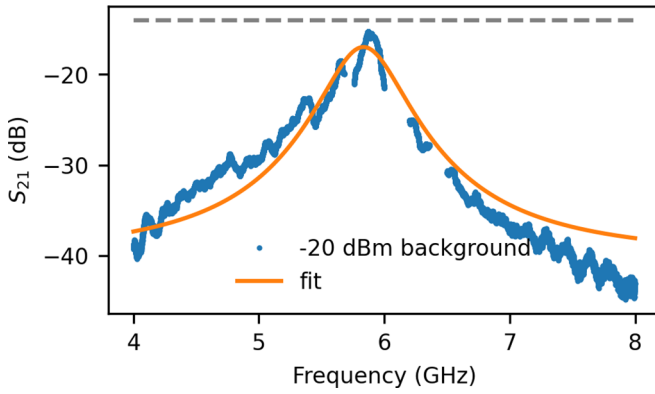


FIG. 12. Box mode. S_{21} transmission spectrum over the accessible frequency range 4–8 GHz with SSH spectrum removed (blue). A Lorentzian fit highlights the presence of a box mode (orange). The dashed gray line indicates the expected transmission given the input attenuation and output amplification.

transmission with a finer modulation and with a maximal transmission around 6 GHz. We attribute the resonance-like peak at around 6 GHz to a spurious feature hosted by the PCB enclosure spanning between the two test ports S and D, which acts as a band pass filter in parallel to the SSH chain, which in turn affects the overall transmission. We also observe that the transmission spectrum recorded in several experimental runs and on different samples, but within the same enclosure differs from the expected transmission spectrum. We highlight the resemblance of the transmission spectrum with a broad band resonator with a fit to a Lorentzian (orange). The finer modulation of the transmission probably arises from impedance mismatches along the lines connecting to the measurement electronics. To simplify the data analysis in the presence of the broad spectral feature, we obtain a linearly interpolated background transmission spectrum to which we normalize the measurement data to better identify the transmission peaks and dips of the SSH chain spectrum.

While we cannot extract the exact effective inductance and capacitance leading to the spurious feature formed by the enclosure, we can approximate its effect in a lumped element simulation in which we assume a resonator in parallel to the

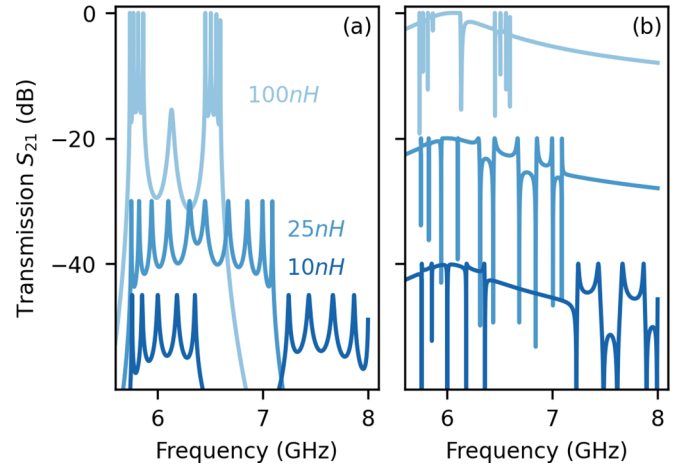


FIG. 13. Lumped element simulation of the three regimes topological, normal, trivial for different tuning scenarios. (a) Expected, ideal SSH chain spectrum for a joint synchronous sweep of L_v . (b) Same device tuning as in (a), but accounting for the presence of a box mode modelled as transmission resonator in parallel to the SSH chain. Note that all spectra per panel are offset for better visibility.

SSH chain. The results of these lumped element simulations are presented in Fig. 13(a) for the ideal case and in Fig. 13(b) for the case in presence of a spurious resonance. In the ideal case, we expect two, or three well defined bands with in total 10 modes and otherwise suppressed background transmission. However, a spurious mode yields a higher overall transmission due its band pass feature and distorts the measured line shape of the modes due to its capacitive contribution on the rising edge and its inductive contribution on the falling edge. Consequently, the bulk modes appear as dips and peaks and the mid gap modes in the topological state appear as deep dip with a shallow peak in the center. The feature, which we modelled for simplicity as a single mode, does not affect the SSH chain, but it does complicate the interpretation of the overall transmission spectrum. To overcome the effect, a new sample enclosure should be carefully designed [90]. Going beyond the current experiment, one could also intentionally coupled a SSH chain to a resonator as described in Ref. [33].

- [1] A. Kitaev and C. Laumann, Topological phases and quantum-computation, [arXiv:0904.2771](https://arxiv.org/abs/0904.2771).
- [2] J. D. Sau and S. D. Sarma, Realizing a robust practical majorana chain in a quantum-dot-superconductor linear array, *Nat. Commun.* **3**, 964 (2012).
- [3] W. P. Su, J. R. Schrieffer, and A. J. Heeger, Solitons in polyacetylene, *Phys. Rev. Lett.* **42**, 1698 (1979).
- [4] M. Z. Hasan and C. L. Kane, Colloquium: Topological insulators, *Rev. Mod. Phys.* **82**, 3045 (2010).
- [5] J. K. Asbóth, L. Oroszlány, and A. Pályi, *A Short Course on Topological Insulators* (Springer International, Cham, 2016).
- [6] N. Batra and G. Sheet, Physics with coffee and doughnuts, *Resonance* **25**, 765 (2020).
- [7] N. Delnour, A. Bissonnette, H. Eleuch, R. MacKenzie, and M. Hilke, Scanning qubit probe of edge states in a topological insulator, *Phys. Lett. A* **466**, 128716 (2023).
- [8] G. Jin and E. Greplova, Topological entanglement stabilization in superconducting quantum circuits, *Phys. Rev. Res.* **5**, 023088 (2023).
- [9] F. Mei, G. Chen, L. Tian, S.-L. Zhu, and S. Jia, Robust quantum state transfer via topological edge states in superconducting qubit chains, *Phys. Rev. A* **98**, 012331 (2018).
- [10] E. Kim, X. Zhang, V. S. Ferreira, J. Banker, J. K. Iverson, A. Siphigil, M. Bello, A. González-Tudela, M. Mirhosseini, and O. Painter, Quantum electrodynamics in a topological waveguide, *Phys. Rev. X* **11**, 011015 (2021).

- [11] C. Vega, M. Bello, D. Porras, and A. González-Tudela, Qubit-photon bound states in topological waveguides with long-range hoppings, *Phys. Rev. A* **104**, 053522 (2021).
- [12] L.-N. Zheng, X. Yi, and H.-F. Wang, Engineering a phase-robust topological router in a dimerized superconducting-circuit lattice with long-range hopping and chiral symmetry, *Phys. Rev. Appl.* **18**, 054037 (2022).
- [13] D.-A. Galeano, X.-X. Zhang, and J. Mahecha, Topological circuit of a versatile non-Hermitian quantum system, *Sci. China Phys. Mech. Astron.* **65**, 217211 (2022).
- [14] M. Zelenayova and E. J. Bergholtz, Non-Hermitian extended midgap states and bound states in the continuum, *Appl. Phys. Lett.* **124**, 041105 (2024).
- [15] I.-F. Io, C.-Y. Huang, J.-S. You, H.-C. Chang, and H. chung Kao, Quasi-Hermitian extended SSH models, [arXiv:2308.09874](https://arxiv.org/abs/2308.09874).
- [16] M. Kiczynski, S. K. Gorman, H. Geng, M. B. Donnelly, Y. Chung, Y. He, J. G. Keizer, and M. Y. Simmons, Engineering topological states in atom-based semiconductor quantum dots, *Nature (Lond.)* **606**, 694 (2022).
- [17] S. de Léséleuc, V. Lienhard, P. Scholl, D. Barredo, S. Weber, N. Lang, H. P. Büchler, T. Lahaye, and A. Browaeys, Observation of a symmetry-protected topological phase of interacting bosons with rydberg atoms, *Science* **365**, 775 (2019).
- [18] V. D. Pham, Y. Pan, S. C. Erwin, F. von Oppen, K. Kanisawa, and S. Fölsch, Topological states in dimerized quantum-dot chains created by atom manipulation, *Phys. Rev. B* **105**, 125418 (2022).
- [19] R.-J. Ren, Y.-H. Lu, Z.-K. Jiang, J. Gao, W.-H. Zhou, Y. Wang, Z.-Q. Jiao, X.-W. Wang, A. S. Solntsev, and X.-M. Jin, Topologically protecting squeezed light on a photonic chip, *Photon. Res.* **10**, 456 (2022).
- [20] Y. Liu, W. Cao, W. Chen, H. Wang, L. Yang, and X. Zhang, Fully integrated topological electronics, *Sci. Rep.* **12**, 13410 (2022).
- [21] T. Iizuka, H. Yuan, Y. Mita, A. Higo, S. Yasunaga, and M. Ezawa, Experimental demonstration of position-controllable topological interface states in high-frequency kitaev topological integrated circuits, *Commun. Phys.* **6**, 279 (2023).
- [22] X. Zhou, W. Zhang, H. Sun, and X. Zhang, Observation of flat-band localization and topological edge states induced by effective strong interactions in electrical circuit networks, *Phys. Rev. B* **107**, 035152 (2023).
- [23] A. Blais, A. L. Grimsmo, S. M. Girvin, and A. Wallraff, Circuit quantum electrodynamics, *Rev. Mod. Phys.* **93**, 025005 (2021).
- [24] S. John and J. Wang, Quantum electrodynamics near a photonic band gap: Photon bound states and dressed atoms, *Phys. Rev. Lett.* **64**, 2418 (1990).
- [25] Y. Liu and A. A. Houck, Quantum electrodynamics near a photonic bandgap, *Nat. Phys.* **13**, 48 (2017).
- [26] M. Mirhosseini, E. Kim, V. S. Ferreira, M. Kalaei, A. Sipahigil, A. J. Keller, and O. Painter, Superconducting metamaterials for waveguide quantum electrodynamics, *Nat. Commun.* **9**, 3706 (2018).
- [27] J. Puertas Martínez, S. Léger, N. Gheeraert, R. Dassonneville, L. Planat, F. Foughi, Y. Krupko, O. Buisson, C. Naud, W. Hasch-Guichard, S. Florens, I. Snyman, and N. Roch, A tunable Josephson platform to explore many-body quantum optics in circuit-QED, *npj Quantum Inf.* **5**, 19 (2019).
- [28] M. Bello, G. Platero, J. I. Cirac, and A. González-Tudela, Unconventional quantum optics in topological waveguide QED, *Sci. Adv.* **5**, eaaw0297 (2019).
- [29] J. D. Brehm, A. N. Poddubny, A. Stehli, T. Wolz, H. Rotzinger, and A. V. Ustinov, Waveguide bandgap engineering with an array of superconducting qubits, *npj Quantum Mater.* **6**, 10 (2021).
- [30] V. S. Ferreira, J. Banker, A. Sipahigil, M. H. Matheny, A. J. Keller, E. Kim, M. Mirhosseini, and O. Painter, Collapse and revival of an artificial atom coupled to a structured photonic reservoir, *Phys. Rev. X* **11**, 041043 (2021).
- [31] W. Nie and Y.-x. Liu, Bandgap-assisted quantum control of topological edge states in a cavity, *Phys. Rev. Res.* **2**, 012076(R) (2020).
- [32] M. Scigliuzzo, G. Calajò, F. Ciccarello, D. Perez Lozano, A. Bengtsson, P. Scarlino, A. Wallraff, D. Chang, P. Delsing, and S. Gasparinetti, Controlling atom-photon bound states in an array of Josephson-Junction resonators, *Phys. Rev. X* **12**, 031036 (2022).
- [33] O. Dmytruk and M. Schirò, Controlling topological phases of matter with quantum light, *Commun. Phys.* **5**, 271 (2022).
- [34] Y. Ke, J. Huang, W. Liu, Y. Kivshar, and C. Lee, Topological inverse band theory in waveguide quantum electrodynamics, *Phys. Rev. Lett.* **131**, 103604 (2023).
- [35] C. H. Lee, S. Imhof, C. Berger, F. Bayer, J. Brehm, L. W. Molenkamp, T. Kiessling, and R. Thomale, Topoelectrical circuits, *Commun. Phys.* **1**, 39 (2018).
- [36] V. Jouanny, S. Frasca, V. J. Weibel, L. Peyruchat, M. Scigliuzzo, F. Oppliger, F. D. Palma, D. Sbroggio, G. Beaulieu, O. Zilberberg, and P. Scarlino, Band engineering and study of disorder using topology in compact high kinetic inductance cavity arrays, [arXiv:2403.18150](https://arxiv.org/abs/2403.18150).
- [37] T. Zhang, J. Hu, and X. Qiu, Topological waveguide quantum sensors, [arXiv:2311.01370](https://arxiv.org/abs/2311.01370).
- [38] P. Pakkiam, N. P. Kumar, M. Pletyukhov, and A. Fedorov, Qubit-controlled directional edge states in waveguide QED, *npj Quantum Inf.* **9**, 53 (2023).
- [39] Y. Wang, H. Xu, X. Deng, T. Liew, S. Ghosh, and Q. Xiong, Topological single-photon emission from quantum emitter chains, *npj Quantum Inf.* **10**, 13 (2024).
- [40] X. Zhang, E. Kim, D. K. Mark, S. Choi, and O. Painter, A superconducting quantum simulator based on a photonic-bandgap metamaterial, *Science* **379**, 278 (2023).
- [41] A. H. Karamlou, J. Braumüller, Y. Yanay, A. Di Paolo, P. M. Harrington, B. Kannan, D. Kim, M. Kjaergaard, A. Melville, S. Muschinske, B. M. Niedzielski, A. Vepsäläinen, R. Winik, J. L. Yoder, M. Schwartz, C. Tahan, T. P. Orlando, S. Gustavsson, and W. D. Oliver, Quantum transport and localization in 1d and 2d tight-binding lattices, *npj Quantum Inf.* **8**, 35 (2022).
- [42] M. A. Beck, M. Selvanayagam, A. Carniol, S. Cairns, and C. P. Mancini, Wideband Josephson parametric isolator, *Phys. Rev. Appl.* **20**, 034054 (2023).
- [43] A. Palacios-Laloy, F. Nguyen, F. Mallet, P. Bertet, D. Vion, and D. Esteve, Tunable resonators for quantum circuits, *J. Low Temp. Phys.* **151**, 1034 (2008).
- [44] Y. Chen, C. Neill, P. Roushan, N. Leung, M. Fang, R. Barends, J. Kelly, B. Campbell, Z. Chen, B. Chiaro, A. Dunsworth, E. Jeffrey, A. Megrant, J. Y. Mutus, P. J. J. O'Malley, C. M. Quintana, D. Sank, A. Vainsencher, J. Wenner, T. C. White

- et al.*, Qubit architecture with high coherence and fast tunable coupling, *Phys. Rev. Lett.* **113**, 220502 (2014).
- [45] P. Roushan, C. Neill, J. Tangpanitanon, V. M. Bastidas, A. Megrant, R. Barends, Y. Chen, Z. Chen, B. Chiaro, A. Dunsworth, A. Fowler, B. Foxen, M. Giustina, E. Jeffrey, J. Kelly, E. Lucero, J. Mutus, M. Neeley, C. Quintana, D. Sank *et al.*, Spectroscopic signatures of localization with interacting photons in superconducting qubits, *Science* **358**, 1175 (2017).
- [46] O. Naaman, M. O. Abutaleb, C. Kirby, and M. Rennie, On-chip Josephson junction microwave switch, *Appl. Phys. Lett.* **108**, 112601 (2016).
- [47] M. R. Vissers, J. Hubmayr, M. Sandberg, S. Chaudhuri, C. Bockstiegel, and J. Gao, Frequency-tunable superconducting resonators via nonlinear kinetic inductance, *Appl. Phys. Lett.* **107**, 062601 (2015).
- [48] M. Xu, X. Han, W. Fu, C.-L. Zou, and H. X. Tang, Frequency-tunable high-Q superconducting resonators via wireless control of nonlinear kinetic inductance, *Appl. Phys. Lett.* **114**, 192601 (2019).
- [49] D. J. Parker, M. Savytskyi, W. Vine, A. Laucht, T. Duty, A. Morello, A. L. Grimsmo, and J. J. Pla, Degenerate parametric amplification via three-wave mixing using kinetic inductance, *Phys. Rev. Appl.* **17**, 034064 (2022).
- [50] D. M. Abrams, N. Didier, S. A. Caldwell, B. R. Johnson, and C. A. Ryan, Methods for measuring magnetic flux crosstalk between tunable transmons, *Phys. Rev. Appl.* **12**, 064022 (2019).
- [51] X. Dai, D. M. Tennant, R. Trappen, A. J. Martinez, D. Melanson, M. A. Yurtalan, Y. Tang, S. Novikov, J. A. Grover, S. M. Disseler, J. I. Basham, R. Das, D. K. Kim, A. J. Melville, B. M. Niedzielski, S. J. Weber, J. L. Yoder, D. A. Lidar, and A. Lupascu, Calibration of flux crosstalk in large-scale flux-tunable superconducting quantum circuits, *PRX Quantum* **2**, 040313 (2021).
- [52] C. N. Barrett, A. H. Karamlou, S. E. Muschinske, I. T. Rosen, J. Braumüller, R. Das, D. K. Kim, B. M. Niedzielski, M. Schuldt, K. Serniak, M. E. Schwartz, J. L. Yoder, T. P. Orlando, S. Gustavsson, J. A. Grover, and W. D. Oliver, Learning-based calibration of flux crosstalk in transmon qubit arrays, *Phys. Rev. Appl.* **20**, 024070 (2023).
- [53] A. Valenti, E. van Nieuwenburg, S. Huber, and E. Greplova, Hamiltonian learning for quantum error correction, *Phys. Rev. Res.* **1**, 033092 (2019).
- [54] G. de Lange, B. van Heck, A. Bruno, D. J. van Woerkom, A. Geresdi, S. R. Plissard, E. P. A. M. Bakkers, A. R. Akhmerov, and L. DiCarlo, Realization of microwave quantum circuits using hybrid superconducting-semiconducting nanowire Josephson elements, *Phys. Rev. Lett.* **115**, 127002 (2015).
- [55] L. Casparis, N. J. Pearson, A. Kringhøj, T. W. Larsen, F. Kuemmeth, J. Nygård, P. Krogstrup, K. D. Petersson, and C. M. Marcus, Voltage-controlled superconducting quantum bus, *Phys. Rev. B* **99**, 085434 (2019).
- [56] A. Hertel, M. Eichinger, L. O. Andersen, D. M. T. van Zanten, S. Kallatt, P. Scarlino, A. Kringhøj, J. M. Chavez-Garcia, G. C. Gardner, S. Gronin, M. J. Manfra, A. Gyenis, M. Kjaergaard, C. M. Marcus, and K. D. Petersson, Gate-tunable transmon using selective-area-grown superconductor-semiconductor hybrid structures on silicon, *Phys. Rev. Appl.* **18**, 034042 (2022).
- [57] L. J. Splitthoff, A. Bargerbos, L. Grünhaupt, M. Pita-Vidal, J. J. Wesdorp, Y. Liu, A. Kou, C. K. Andersen, and B. van Heck, Gate-tunable kinetic inductance in proximitized nanowires, *Phys. Rev. Appl.* **18**, 024074 (2022).
- [58] D. Phan, P. Falthansl-Scheinecker, U. Mishra, W. M. Strickland, D. Langone, J. Shabani, and A. P. Higginbotham, Gate-tunable superconductor-semiconductor parametric amplifier, *Phys. Rev. Appl.* **19**, 064032 (2023).
- [59] L. J. Splitthoff, J. J. Wesdorp, M. Pita-Vidal, A. Bargerbos, Y. Liu, and C. K. Andersen, Gate-tunable kinetic inductance parametric amplifier, *Phys. Rev. Appl.* **21**, 014052 (2024).
- [60] I. Mondragon-Shem, T. L. Hughes, J. Song, and E. Prodan, Topological criticality in the chiral-symmetric AIII class at strong disorder, *Phys. Rev. Lett.* **113**, 046802 (2014).
- [61] J. Song and E. Prodan, AIII and BDI topological systems at strong disorder, *Phys. Rev. B* **89**, 224203 (2014).
- [62] T. Rakovszky, J. K. Asbóth, and A. Alberti, Detecting topological invariants in chiral symmetric insulators via losses, *Phys. Rev. B* **95**, 201407(R) (2017).
- [63] E. Prodan and H. Schulz-Baldes, *Bulk and Boundary Invariants for Complex Topological Insulators, From K-theory to Physics*, Mathematical Physics Studies (Springer, Cham, 2016).
- [64] M. W. A. de Moor, J. D. S. Bommer, D. Xu, G. W. Winkler, A. E. Antipov, A. Bargerbos, G. Wang, N. van Loo, R. L. M. O. het Veld, S. Gazibegovic, D. Car, J. A. Logan, M. Pendharkar, J. S. Lee, E. P. A. M. Bakkers, C. J. Palmstrøm, R. M. Lutchyn, L. P. Kouwenhoven, and H. Zhang, Electric field tunable superconductor-semiconductor coupling in Majorana nanowires, *New J. Phys.* **20**, 103049 (2018).
- [65] L. Casparis, M. R. Connolly, M. Kjaergaard, N. J. Pearson, A. Kringhøj, T. W. Larsen, F. Kuemmeth, T. Wang, C. Thomas, S. Gronin, G. C. Gardner, M. J. Manfra, C. M. Marcus, and K. D. Petersson, Superconducting gatemon qubit based on a proximitized two-dimensional electron gas, *Nat. Nanotechnol.* **13**, 915 (2018).
- [66] M. Pita-Vidal, A. Bargerbos, R. Žitko, L. J. Splitthoff, L. Grünhaupt, J. J. Wesdorp, Y. Liu, L. P. Kouwenhoven, R. Aguado, B. van Heck, A. Kou, and C. K. Andersen, Direct manipulation of a superconducting spin qubit strongly coupled to a transmon qubit, *Nat. Phys.* **19**, 1110 (2023).
- [67] S. Longhi, Probing one-dimensional topological phases in waveguide lattices with broken chiral symmetry, *Opt. Lett.* **43**, 4639 (2018).
- [68] B. Pérez-González, M. Bello, A. Gómez-León, and G. Platero, Interplay between long-range hopping and disorder in topological systems, *Phys. Rev. B* **99**, 035146 (2019).
- [69] M. Scollon and M. P. Kennett, Persistence of chirality in the Su-Schrieffer-Heeger model in the presence of on-site disorder, *Phys. Rev. B* **101**, 144204 (2020).
- [70] Z. Xia, J. Huo, Z. Li, J. Ying, Y. Liu, X.-Y. Tang, Y. Wang, M. Chen, D. Pan, S. Zhang, Q. Liu, T. Li, L. Li, K. He, J. Zhao, R. Shang, and H. Zhang, Gate-compatible circuit QED in a three-dimensional cavity architecture, *Phys. Rev. Appl.* **21**, 034031 (2024).
- [71] T. W. Larsen, M. E. Gershenson, L. Casparis, A. Kringhøj, N. J. Pearson, R. P. G. McNeil, F. Kuemmeth, P. Krogstrup, K. D. Petersson, and C. M. Marcus, Parity-protected superconductor-semiconductor qubit, *Phys. Rev. Lett.* **125**, 056801 (2020).
- [72] T. Dvir, G. Wang, N. van Loo, C.-X. Liu, G. P. Mazur, A. Bordin, S. L. D. ten Haaf, J.-Y. Wang, D. van Driel, F. Zlatelli, X. Li, F. K. Malinowski, S. Gazibegovic, G. Badawy, E. P. A. M. Bakkers, M. Wimmer, and L. P. Kouwenhoven, Realization of a

- minimal kitaev chain in coupled quantum dots, *Nature (Lond.)* **614**, 445 (2023).
- [73] D. M. Pino, R. S. Souto, and R. Aguado, Minimal Kitaev-Transmon qubit based on double quantum dots, *Phys. Rev. B* **109**, 075101 (2024).
- [74] X.-J. Luo, X.-H. Pan, C.-X. Liu, and X. Liu, Higher-order topological phases emerging from Su-Schrieffer-Heeger stacking, *Phys. Rev. B* **107**, 045118 (2023).
- [75] W. M. Strickland, L. J. Baker, J. Lee, K. Dindial, B. H. Elfeky, P. J. Strohbeen, M. Hatefipour, P. Yu, I. Levy, J. Issokson, V. E. Manucharyan, and J. Shabani, Characterizing losses in InAs two-dimensional electron gas-based gatemon qubits, *Phys. Rev. Res.* **6**, 023094 (2024).
- [76] M. Zaimi, C. Boudreault, N. Baspin, N. Delnour, H. Eleuch, R. MacKenzie, and M. Hilke, Detecting topological edge states with the dynamics of a qubit, *Phys. Lett. A* **388**, 127035 (2021).
- [77] Y. Hadad, J. C. Soric, A. B. Khanikaev, and A. Alù, Self-induced topological protection in nonlinear circuit arrays, *Nat. Electron.* **1**, 178 (2018).
- [78] J. M. P. Nair, Nonlinear construction of topological SSH models, *arXiv:2211.16440*.
- [79] M. J. Rice and E. J. Mele, Elementary excitations of a linearly conjugated diatomic polymer, *Phys. Rev. Lett.* **49**, 1455 (1982).
- [80] S. Aubry and G. André, Analyticity breaking and Anderson localization in incommensurate lattices, *Ann. Isr. Phys. Soc.* **3**, 18 (1980).
- [81] Y. E. Kraus, Y. Lahini, Z. Ringel, M. Verbin, and O. Zeitler, Topological states and adiabatic pumping in quasicrystals, *Phys. Rev. Lett.* **109**, 106402 (2012).
- [82] H. Li, Y.-Y. Wang, Y.-H. Shi, K. Huang, X. Song, G.-H. Liang, Z.-Y. Mei, B. Zhou, H. Zhang, J.-C. Zhang, S. Chen, Z.-Y. Yang, Z. Xiang, K. Xu, D. Zheng, and H. Fan, Observation of critical phase transition in a generalized Aubry-André-Harper model with superconducting circuits, *npj Quantum Inf.* **9**, 40 (2023).
- [83] Y. Zhang, Y.-Q. Ge, and Y. xi Liu, Simulation of kitaev model using one-dimensional chain of superconducting qubits and environmental effect on topological states, *arXiv:2302.03834*.
- [84] L. Splitthoff, M. Carrera Belo, G. Jin, Y. Liu, E. Greplova, and C. K. Andersen, Data and code underlying the paper: “Gate-tunable phase transition in a bosonic Su-Schrieffer-Heeger chain”, Version 1, 4TU.ResearchData, dataset, <https://doi.org/10.4121/9df557c0-a0fc-458b-ae6a-d973b7974ced.v1> (2024).
- [85] U. Vool and M. Devoret, Introduction to quantum electromagnetic circuits, *Int. J. Circ. Theory Appl.* **45**, 897 (2017).
- [86] S. Ryu, A. P. Schnyder, A. Furusaki, and A. W. Ludwig, Topological insulators and superconductors: Tenfold way and dimensional hierarchy, *New J. Phys.* **12**, 065010 (2010).
- [87] J. K. Asbóth, L. Oroszlány, and A. Pályi, *A Short Course on Topological Insulators*, Lecture Notes in Physics, Vol. 919 (Springer, Cham, 2016).
- [88] A. P. Schnyder, S. Ryu, and A. W. W. Ludwig, Lattice model of a three-dimensional topological singlet superconductor with time-reversal symmetry, *Phys. Rev. Lett.* **102**, 196804 (2009).
- [89] P. Krogstrup, N. L. B. Ziino, W. Chang, S. Albrecht, M. H. Madsen, E. Johnson, J. Nygård, C. M. Marcus, and T. S. Jepsen, Epitaxy of semiconductor-superconductor nanowires, *Nat. Mater.* **14**, 400 (2015).
- [90] S. Huang, B. Lienhard, G. Calusine, A. Vepsäläinen, J. Braumüller, D. K. Kim, A. J. Melville, B. M. Niedzielski, J. L. Yoder, B. Kannan, T. P. Orlando, S. Gustavsson, and W. D. Oliver, Microwave package design for superconducting quantum processors, *PRX Quantum* **2**, 020306 (2021).